

The Gallium Intermetallics $REPdGa_3$ ($RE = La, Ce, Pr, Nd, Sm, Eu$) with $SrPdGa_3$ -type Structure

Stefan Seidel^a, Oliver Niehaus^a, Samir F. Matar^b, Oliver Janka^a, Birgit Gerke^a,
Ute Ch. Rodewald^a, and Rainer Pöttgen^a

^a Institut für Anorganische und Analytische Chemie, Universität Münster, Corrensstrasse 30,
48149 Münster, Germany

^b CNRS, Université de Bordeaux, ICMCB, 87 Avenue Dr. A. Schweitzer, 33608 Pessac-Cedex,
France

Reprint requests to R. Pöttgen. E-mail: pottgen@uni-muenster.de

Z. Naturforsch. **2014**, *69b*, 1105 – 1118 / DOI: 10.5560/ZNB.2014-4119

Received June 6, 2014

Dedicated to Professor Hubert Schmidbaur on the occasion of his 80th birthday

The gallium-rich intermetallic phases $REPdGa_3$ ($RE = La, Ce, Pr, Nd, Sm, Eu$) were obtained by arc-melting of the elements and subsequent annealing for crystal growth. The samples were studied by X-ray diffraction on powders and single crystals. The structures of three crystals were refined from X-ray diffractometer data: $SrPdGa_3$ type, $Cmcm$, $a = 634.3(1)$, $b = 1027.2(1)$, $c = 593.5(1)$ pm, $wR = 0.0621$, 380 F^2 values, 20 variables for $CePd_{0.80(4)}Ga_{3.20(4)}$, $a = 635.9(1)$, $b = 1027.5(1)$, $c = 592.0(1)$ pm, $wR = 0.1035$, 457 F^2 values, 19 variables for $CePdGa_3$, and $a = 640.7(1)$, $b = 1038.2(1)$, $c = 593.7(1)$ pm, $wR = 0.0854$, 489 F^2 values, 19 variables for $EuPdGa_3$. The $REPdGa_3$ gallides are orthorhombic superstructure variants of the aristotype $ThCr_2Si_2$. The palladium and gallium atoms build up polyanionic $[PdGa_3]^{δ-}$ networks with Pd–Ga and Ga–Ga distances of 248–254 and 266–297 pm, respectively, in $EuPdGa_3$. The rare earth atoms fill cavities within the polyanionic networks. They are coordinated by five palladium and twelve gallium atoms. Taking $CePdGa_3$ as an illustrative representative, the band structure calculations show largely dispersive itinerant s , p bands and little dispersive d (Pd) and f (Ce) bands, the latter crossing the Fermi level at large magnitude leading to magnetic instability in a spin-degenerate state and a subsequent antiferromagnetic ground state with a small moment of $\pm 0.36 \mu_B$ on Ce. The bonding characteristics indicate a prevailing Ce–Ga bonding versus Pd–Ga and Ce–Pd. Temperature-dependent magnetic susceptibility and ^{151}Eu Mössbauer spectroscopic measurements point to stable trivalent lanthanum, cerium, praseodymium, and neodymium, but divalent europium. $SmPdGa_3$ shows intermediate valence. Antiferromagnetic ordering occurs at $T_N = 5.1(5)$, $7.0(5)$, $6.3(5)$, $11.9(5)$, and $23.0(5)$ for $RE = Ce, Pr, Nd, Sm, \text{ and } Eu$, respectively.

Key words: Gallide, Rare Earth Compounds, $SrPdGa_3$ Type, Magnetic Properties, Mössbauer Spectroscopy

Introduction

Among the many superstructures of the $BaAl_4/ThCr_2Si_2$ family (space group $I4/mmm$) [1–3], those of the $CaBe_2Ge_2$ (space group $P4/nmm$) [4] and $BaNiSn_3$ ($I4mm$) [5] types have by far the most representatives. These two superstructures allow different ordering patterns within the polyanionic networks. In the $CaBe_2Ge_2$ type, every other layer of tetrahedra shows inverse occupancy, leading to Be–Ge bonding between the layers, while it is Al–Al, respectively Si–Si bonding in the aristotype. The change in com-

position in $BaNiSn_3$ requests a symmetry reduction to a non-centrosymmetric space group in order to enable nickel-tin ordering. Both superstructures have several degrees of freedom in order to react on geometric constraints: (i) variation of the crystallographic a and c lattice parameters and (ii) shifts in the z coordinates of some of the atoms. These tolerances are probably the main reason for the large number of representatives.

If the geometrical and electronic requirements cannot be realized, further distortions occur along with another step of symmetry reduction. Such superstructure variants often account for a special requirement of

a given composition, and only few representatives (if at all) occur. Such a situation has recently been described for the superstructures of $BaNi_2Si_2$ and $SrPdGa_3$ [6] which show two different patterns of orthorhombic distortions. So far, $BaNi_2Si_2$ is the only representative of this type, while rare earth-based isotypic compounds have been observed for the $SrPdGa_3$ type. Gallium-rich intermetallics of the solid solutions $REPd_xGa_{4-x}$ have been studied for $RE = La, Ce, Pr, Nd, Sm$ [7]. The $BaAl_4$ -type subcell structure, space group $I4/mmm$, has been assigned on the basis of powder X-ray diffraction data for samples up to $x = 0.85$ for $RE = Pr, Nd, Sm$ and up to $x = 1$ for $RE = La$. Herein we report on samples with $x = 1$ for $RE = La, Ce, Pr, Nd, Sm$, and Eu which show full palladium-gallium ordering, *i. e.* isotypism with $SrPdGa_3$. Besides single-crystal X-ray diffraction we characterized these gallium-rich compounds through magnetic susceptibility measurements and $EuPdGa_3$ also by ^{151}Eu Mössbauer spectroscopy. Lastly we used computations within the well-established quantum-theoretical DFT (density functional theory) framework [8, 9] to further assess experimental results with the electronic structure and chemical bonding properties.

Experimental

Synthesis

Starting materials for the synthesis of the $REPdGa_3$ ($RE = La, Ce, Pr, Nd, Sm, Eu$) samples were pieces of the sublimed rare earth elements (Smart Elements), palladium sheets (Allgosi) and gallium lumps (Johnson Matthey), all with stated purities better than 99.9%. The rare earth elements were cut into suitable pieces and kept in Schlenk tubes under argon prior to the reactions. The argon was purified with a titanium sponge (900 K), molecular sieves and silica gel. A small laboratory arc furnace was used for reaction of the metals [10]. The elements were weighted in the ideal atomic ratio of 1 : 1 : 3 and arc-melted under an argon atmosphere of 800 mbar in a water-cooled copper crucible.

The obtained buttons were remelted several times to ensure homogeneity. For physical property measurements some of the $REPdGa_3$ samples ($RE = La, Ce, Sm, Eu$) were additionally annealed to increase their phase purity. Therefore, the obtained buttons were sealed in evacuated quartz ampoules. Subsequently the samples of $SmPdGa_3$ and $EuPdGa_3$ were heated within 2 h to 700 K. This temperature was kept for 3 d. The annealing process was stopped by quenching in cold water. The sealed quartz ampoules containing the $LaPdGa_3$ and $CePdGa_3$ samples were placed in the water-cooled sample chamber of a high-frequency furnace (Typ TIG 5/300, Hüttinger Elektronik, Freiburg, Germany) [11] and heated slightly below the melting point of the respective sample. This temperature was kept for 10 min. Subsequently the power of the furnace was reduced by 30%. The samples were kept at this temperature for another two hours and then cooled to room temperature by switching off the power supply. All samples showed metallic luster and were stable at air over weeks.

EDX data

Semiquantitative EDX analyses of the single-crystal fragments which were used for the data collection was carried out using a Zeiss EVO MA10 scanning electron microscope with CeO_2 , EuF_3 , Pd and GaP as standards. The irregularly shaped crystals contained no impurity elements heavier than sodium, and the experimentally determined compositions were close to the ideal ones.

X-Ray diffraction

The $REPdGa_3$ bulk samples were characterized by powder X-ray diffraction using a Guinier camera equipped with an image plate system (Fujifilm, BAS-1800) using $CuK_{\alpha 1}$ radiation and α -quartz ($a = 491.30$, $c = 540.46$ pm) as an internal standard. The orthorhombic lattice parameters (Table 1) have been derived from least-squares refinements of the powder data. The experimental patterns were compared to calculated ones [12] to ensure correct indexing.

Irregularly shaped crystal fragments of $CePd_{0.8}Ga_{3.2}$, $CePdGa_3$ and $EuPdGa_3$ were obtained by mechanical fragmentation of the annealed samples. These fragments were

Compound	a (pm)	b (pm)	c (pm)	V (nm ³)	Reference
$LaPdGa_3$	638.4(2)	1034.1(3)	596.8(2)	0.3940	this work
$CePd_{0.80(4)}Ga_{3.20(4)}$ ^a	634.3(1)	1027.2(1)	593.5(1)	0.3867	this work
$CePdGa_3$	635.9(1)	1027.5(1)	591.98(9)	0.3868	this work
$PrPdGa_3$	635.0(1)	1024.3(1)	589.0(1)	0.3831	this work
$NdPdGa_3$	632.3(2)	1023.0(2)	587.1(1)	0.3798	this work
$SmPdGa_3$	632.9(1)	1018.0(1)	582.7(1)	0.3754	this work
$EuPdGa_3$	640.7(1)	1038.2(2)	593.7(1)	0.3949	this work
$SrPdGa_3$	643.7(1)	1044.9(2)	600.4(1)	0.4038	[4]

^a Single-crystal lattice parameters.

Table 1. Lattice parameters of different $REPdGa_3$ compounds ($RE = La, Ce, Pr, Nd, Sm, Eu$).

glued to thin quartz fibers using beeswax. The crystal quality was tested by Laue photographs on a Buerger camera (white molybdenum radiation, image plate technique, Fujifilm, BAS-1800). Intensity data sets of suitable crystals

were collected at room temperature by use of a Stoe IPDS II diffractometer (graphite-monochromatized MoK_α radiation; $\lambda = 71.073$ pm; oscillation mode). Numerical absorption corrections were applied to the data sets. All relevant

Table 2. Crystallographic data and structure refinement for CePd_{0.80(4)}Ga_{3.20(4)}, CePdGa₃ and EuPdGa₃, space group *Cmcm*, $Z = 4$.

Empirical formula	CePd _{0.80(4)} Ga _{3.20(4)}	CePdGa ₃	EuPdGa ₃
Molar mass, g mol ⁻¹	448.2	455.7	467.5
Lattice parameters			
<i>a</i> , pm	634.3(1)	635.9(1)	640.7(1)
<i>b</i> , pm	1027.2(1)	1027.5(1)	1038.2(1)
<i>c</i> , pm	593.5(1)	592.0(1)	593.7(1)
Cell volume, nm ³	$V = 0.3867$	$V = 0.3868$	$V = 0.3949$
Density calcd., g cm ⁻³	7.70	7.82	7.86
Crystal size, μm^3	10 × 30 × 30	10 × 20 × 30	20 × 30 × 40
Detector distance, mm	80	60	60
Exposure time, s	720	720	300
Integr. param. A / B / EMS	12.8 / 1.9 / 0.011	12.8 / 2.3 / 0.012	12.8 / 2.8 / 0.012
Transm. ratio (min/max)	0.396 / 0.727	0.370 / 0.646	0.249 / 0.605
Absorption coeff., mm ⁻¹	36.9	36.5	40.1
$F(000)$, <i>e</i>	776	788	808
θ range, deg	3–32	3–35	3–35
Range in <i>hkl</i>	±9; ±15; +8	±10; ±16; ±9	±10; ±16; +9
No. of reflections	1199	3962	1558
Independent reflections / R_{int}	380 / 0.0663	457 / 0.1296	489 / 0.0629
Reflections with $I > 3\sigma(I)$	246	341	375
Data/parameters	380 / 20	457 / 19	489 / 19
Goodness-of-fit	1.09	2.33	2.09
R / wR for $I > 3\sigma(I)$	0.0302 / 0.0576	0.0482 / 0.1014	0.0387 / 0.0846
R / wR for all data	0.0584 / 0.0621	0.0682 / 0.1035	0.0485 / 0.0854
Extinction coefficient	90(12)	1600(300)	140(20)
Largest diff. peak/hole, $e \text{ \AA}^{-3}$	+2.01 / -2.27	+4.15 / -2.90	+2.62 / -2.48

Table 3. Atom positions and anisotropic displacement parameters (pm²) for CePd_{0.80(4)}Ga_{3.20(4)}, CePdGa₃ and EuPdGa₃. U_{eq} is defined as one third of the trace of the orthogonalized U_{ij} tensor. Coefficients U_{ij} of the anisotropic displacement factor tensor of the atoms are defined by: $-2\pi^2[(ha^*)^2U_{11} + \dots + 2hka^*b^*U_{12}]$. $U_{12} = U_{13} = 0$.

Atom	Wyckoff position	<i>x</i>	<i>y</i>	<i>z</i>	U_{11}	U_{22}	U_{33}	U_{23}	U_{eq}
CePd _{0.80(4)} Ga _{3.20(4)}									
Ce	4 <i>c</i>	0	0.76563(10)	1/4	131(5)	124(5)	111(5)	0	122(3)
<i>M</i> ^a	4 <i>c</i>	0	0.09528(13)	1/4	130(9)	148(9)	150(9)	0	143(5)
Ga1	4 <i>c</i>	0	0.33713(19)	1/4	149(10)	181(10)	107(11)	0	146(6)
Ga2	8 <i>e</i>	0.2832(2)	0	0	130(6)	140(6)	125(6)	5(5)	132(4)
CePdGa ₃									
Ce	4 <i>c</i>	0	0.76565(13)	1/4	104(5)	106(6)	108(5)	0	106(3)
Pd	4 <i>c</i>	0	0.09386(18)	1/4	117(7)	132(8)	151(7)	0	133(4)
Ga1	4 <i>c</i>	0	0.3344(3)	1/4	129(9)	126(12)	127(10)	0	124(6)
Ga2	8 <i>e</i>	0.2834(3)	0	0	112(6)	159(9)	123(7)	7(5)	131(4)
EuPdGa ₃									
Eu	4 <i>c</i>	0	0.76595(9)	1/4	126(4)	106(4)	111(4)	0	114(2)
Pd	4 <i>c</i>	0	0.09574(13)	1/4	122(5)	122(5)	148(7)	0	131(3)
Ga1	4 <i>c</i>	0	0.33502(19)	1/4	146(8)	119(8)	134(10)	0	133(5)
Ga2	8 <i>e</i>	0.2820(2)	0	0	119(5)	145(6)	129(6)	0(5)	131(3)

^a Occupancy: 80(4) % Pd + 20(4) % Ga.

crystallographic data and details of the data collections and evaluations are listed in Table 2.

Structure refinements

Careful analyses of the three data sets revealed *C*-centered orthorhombic lattices, and the systematic extinctions were in accordance with the space group *Cmcm*. Isotypism of the $REPdGa_3$ phases with the recently reported gallide $SrPdGa_3$ [6] was already evident from the Guinier powder patterns. The atomic parameters of $SrPdGa_3$ [6] were taken as starting values, and the three structures were refined on F^2 with anisotropic displacement parameters for all atoms using the JANA2006 [13] routine. Refinement of the occupancy parameters revealed Pd/Ga mixing for one of the 4c sites of the first cerium-containing crystal. This mixed occupancy was then refined as a least-squares variable in the final cycles, leading to the composition $CePd_{0.80(4)}Ga_{3.20(4)}$. The slightly different composition has only marginal influence on the lattice parameters (see Table 1). All other sites were fully occupied within three standard deviations. The final difference Fourier synthesis revealed no significant residual peaks. The final positional parameters and interatomic distances are listed in Tables 3 and 4.

Further details of the crystal structure investigation may be obtained from Fachinformationszentrum Karlsruhe, 76344 Eggenstein-Leopoldshafen, Germany (fax: +49-7247-

808-666; e-mail: crysdata@fiz-karlsruhe.de, http://www.fiz-karlsruhe.de/request_for_deposited_data.html) on quoting the deposition number CSD-427868 ($CePd_{0.80(4)}Ga_{3.20(4)}$), CSD-427867 ($CePdGa_3$) and CSD-427869 ($EuPdGa_3$).

Physical property measurements

The magnetic and heat capacity measurements were carried out on a Quantum Design Physical Property Measurement System (PPMS) using dc-MS and heat capacity options, respectively. Dc magnetic measurements were performed using the VSM (Vibrating Sample Magnetometer) option. For these measurements approximately 20 mg of the powdered samples were packed in a polypropylene capsule and attached to the sample holder rod. For the heat capacity measurement a piece of $CePdGa_3$ (5.428 mg) was fixed to a pre-calibrated heat capacity puck using Apiezon N grease. Magnetic investigations were performed in the temperature range from 2.5 to 305 K with magnetic flux densities up to 80 kOe ($1 \text{ kOe} = 7.96 \times 10^4 \text{ A m}^{-1}$). Heat capacity measurements were done in the temperature range from 2.0 to 310 K.

^{151}Eu Mössbauer spectroscopy

The 21.53 keV transition of ^{151}Eu with an activity of 130 MBq (2% of the total activity of a $^{151}\text{Sm} : \text{EuF}_3$ source) was used for the Mössbauer spectroscopic experiment, which

Table 4. Interatomic distances (pm) for $CePd_{0.80(4)}Ga_{3.20(4)}$, $CePdGa_3$ and $EuPdGa_3$. All distances of the first coordination spheres are listed. Standard deviations are equal or smaller than 0.2 pm.

$CePd_{0.80(4)}Ga_{3.20(4)}$			$CePdGa_3$			$EuPdGa_3$					
Ce:	2	Ga1	315.0	Ce:	2	Ga1	313.3	Eu:	2	Ga1	314.8
	2	Ga1	325.5		2	Ga1	325.7		2	Ga1	328.3
	2	<i>M</i>	329.4		2	Pd	329.3		2	Pd	329.8
	4	Ga2	335.0		4	Ga2	335.2		4	Ga2	337.2
	1	<i>M</i>	338.6		1	Pd	337.2		1	Pd	342.4
	4	Ga2	339.7		4	Ga2	339.7		4	Ga2	343.2
	2	<i>M</i>	362.2		2	Pd	363.7		2	Pd	365.9
<i>M</i> :	1	Ga1	248.4	<i>Pd</i> :	1	Ga1	247.2	<i>Pd</i> :	1	Ga1	248.4
	4	Ga2	252.7		4	Ga2	252.4		4	Ga2	254.1
	2	Ce	329.4		2	Ce	329.3		2	Eu	329.8
	1	Ce	338.6		1	Ce	337.2		1	Eu	342.4
	2	<i>M</i>	355.5		2	Pd	353.3		2	Pd	357.3
	2	Ce	362.2		2	Ce	363.7		2	Eu	365.9
Ga1:	1	<i>M</i>	248.4	Ga1:	1	Pd	247.2	Ga1:	1	Pd	248.4
	4	Ga2	262.5		4	Ga2	264.2		4	Ga2	266.2
	2	Ce	315.0		2	Ce	313.3		2	Eu	314.8
	2	Ce	325.5		2	Ce	325.7		2	Eu	328.3
Ga2:	2	<i>M</i>	252.7	Ga2:	2	Pd	252.4	Ga2:	2	Pd	254.1
	2	Ga1	262.5		2	Ga1	264.2		2	Ga1	266.2
	1	Ga2	275.0		1	Ga2	275.5		1	Ga2	279.3
	2	Ga2	296.7		2	Ga2	296.0		2	Ga2	296.8
	2	Ce	335.0		2	Ce	335.2		2	Eu	337.2
	2	Ce	339.7		2	Ce	339.7		2	Eu	343.2

was conducted in the usual transmission geometry. The measurement was performed with a commercial nitrogen-bath cryostat at 78 K and with a helium-flow cryostat at 5 K. The sample was enclosed in a small PMMA container at a thickness corresponding to about 10 mg Eu cm^{-2} . Fitting of the spectrum was performed with the NORMOS-90 program system [14].

Computational details

All-electron calculations based on DFT with a gradient exchange-correlation function GGA [15] were carried out with the experimental crystal parameters of $CePdGa_3$ for a full description of the electronic and magnetic structures and the chemical bonding properties. They were performed using the full potential augmented spherical wave (ASW) method [16, 17] in a scalar relativistic implementation [18]. In the ASW method, the wave function is expanded in atom-centered augmented spherical waves, which are Hankel functions and numerical solutions of Schrödinger's equation, respectively, outside and inside the so-called augmentation spheres. In the minimal ASW basis set, we chose the outermost shells to represent the valence states, and the matrix elements were constructed using partial waves up to $l_{\text{max}} + 1 = 4$ for Ce, $l_{\text{max}} + 1 = 3$ for Pd and $l_{\text{max}} + 2$ for Ga. Low-energy $Ga(3d^{10})$ states were considered as core states. In order to optimize the basis set, additional augmented spherical waves were placed at carefully selected interstitial sites (IS). Self-consistency was achieved when charge transfer and energy changes between two successive cycles were $\Delta Q < 10^{-8}$ and $\Delta E < 10^{-6} \text{ eV}$, respectively. The Brillouin zone (BZ) integrations were performed using the linear tetrahedron method within the irreducible wedge [19]. The calculations were carried out firstly as spin-degenerate, non spin-polarized (NSP),

followed by spin-polarized (SP) magnetic calculations for both ferromagnetic (SP-F) and antiferromagnetic (SP-AF) long-range ordering for the identification of the ground-state magnetic structure of $CePdGa_3$. A qualitative description of the chemical bonding was obtained based on the overlap population analysis, S_{ij} , with i and j being two chemical species. The crystal orbital overlap population (COOP) criterion was used [20]. In the plots positive, negative and zero COOP values indicate bonding, anti-bonding and non-bonding interactions, respectively. Exemplarily we examined $CePdGa_3$ with NSP, SP-F and SP-AF states.

Discussion

Crystal chemistry

The crystal structure of $SrPdGa_3$ along with the group-subgroup relation in going from the aristotype $BaAl_4/ThCr_2Si_2$ have been discussed in detail in previous work [6]. Herein we focus only on the crystal chemistry of the new gallide $EuPdGa_3$ and the series of $REPd_xGa_{4-x}$ phases with the heavier rare earth elements.

The $REPdGa_3$ gallides are the ordered $x = 1$ members of the solid solutions $REPd_xGa_{4-x}$. The Guinier powder patterns (the one of $CePdGa_3$ is shown exemplarily in Fig. 1) clearly show the characteristic reflections deriving from the superstructure formation. Especially the 200 and 002 reflections show drastically different d spacings. They originate from the 110 subcell reflection due to the strong orthorhombic distortion. Another important point concerns the widths

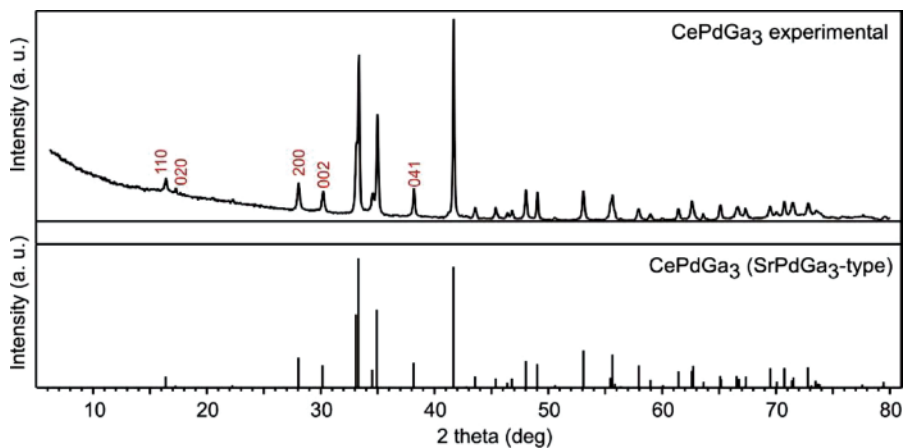


Fig. 1 (color online). Experimental (top) and calculated (bottom) powder patterns for $CePdGa_3$. hkl indices for relevant reflections are marked in red. For details see text.

of the reflections. Comparison of the six $REPdGa_3$ powder patterns shows enhanced half widths for all cerium samples. This is indicative of a distribution of $CePd_{1\pm x}Ga_{3\pm x}$ domains with slightly different composition and/or Pd/Ga disorder in the bulk sample, as is also evident from the $CePd_{0.80(4)}Ga_{3.20(4)}$ crystal. We draw back to this point when discussing the magnetic properties (*vide infra*).

A view of the $EuPdGa_3$ structure approximately along the [101] direction is presented in Fig. 2. The lattice parameters of $EuPdGa_3$ are slightly smaller than those of the strontium compound ($a = 643.7(1)$, $b = 1044.9(2)$, $c = 600.4(1)$ pm) [6]. This is in line with the course of the ionic radii [21] of 112 and 109 pm for Sr^{2+} and Eu^{2+} , respectively.

Within the three-dimensional $[PdGa_3]$ network each palladium atom has five gallium neighbors in distorted square-pyramidal coordination at Pd–Ga distances ranging from 248 to 254 pm, close to the sum of the covalent radii for palladium and gallium of 253 pm [21]. The palladium atoms are well separated from each other within this network. The shortest Pd–Pd distance of 357 pm is certainly not contributing to the bonding. The gallium atoms have between 4 and 5 gallium neighbors at Ga–Ga distances of 266–297 pm. A similar range of Ga–Ga distances occurs in elemental gallium with the typical coordination of 1×244 and 6×270 pm [22].

The europium atoms fill larger cages left by the three-dimensional $[PdGa_3]$ network. Each europium atom has 17 nearest neighbors, 12 gallium and 5 pal-

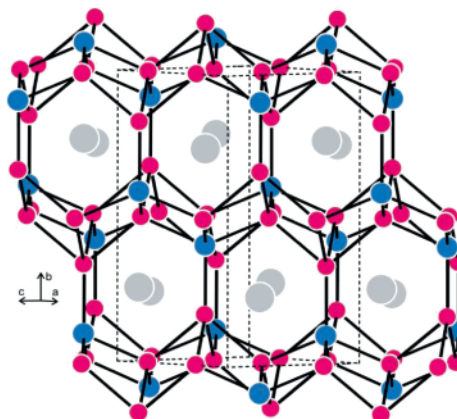


Fig. 2 (color online). The crystal structure of $EuPdGa_3$. Europium, palladium and gallium atoms are drawn as medium-grey, blue and magenta circles, respectively. The three-dimensional $[PdGa_3]$ polyanionic network is emphasized.

ladium atoms. Due to the strong distortion the Eu–Ga and Eu–Pd distances cover the relatively broad range from 315 to 366 pm. Primary bonding proceeds through the shorter Eu–Ga contacts.

Inspection of the Pearson data base [23] for space group $Cmcm$ and the Wyckoff sequence ec^3 reveals that $SrPdGa_3$ [6] and $REPdGa_3$ ($RE = La, Ce, Pr, Nd, Sm, Eu$) are isopointal with $PbSbO_2Cl$ [24–26] and the recently reported zinc-rich compound $LaZn_4$ [27]. Especially the Sb(III) compound with a strong lone-pair effect shows drastic shifts in the lattice as well as in the positional parameters. This causes severe differences

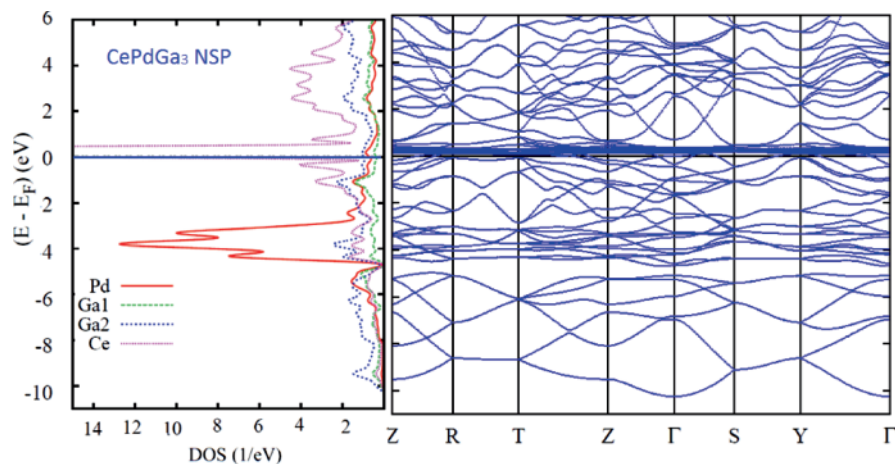


Fig. 3 (color online). Electronic structure of $CePdGa_3$, non magnetic (NSP) calculations: Site projected density of states (DOS) and mirroring band structure along the major direction of the corresponding BZ.

in chemical bonding, and these phases are rather isopointal [28, 29] than isotypic. In the case of intermetallic zinc compounds it will be interesting to test for ordered substitution variants with palladium or other transition metals.

Our phase-analytical work indicated that the $REPdGa_3$ phases with $SrPdGa_3$ structure exist only up to europium. With the heavier rare earth elements orthorhombic La_3Al_{11} -type phases are formed [30].

The main focus of the present manuscript now concerns the magnetic properties of the $REPdGa_3$ phases as well as a ^{151}Eu Mössbauer spectroscopic characterization of the europium phase.

Electronic structure and chemical bonding

The calculations were first carried out considering a spin-degenerate configuration (NSP), translating a non-magnetic state, *i. e.* not a paramagnetic one whose modeling would require a large supercell with random spin orientation over the magnetic sites. At self-consistent energy and charge convergence there is charge redistribution among the valence states of the constituents with a trend to negatively charged Pd and small charge residues ($\sim 0.2e$) to the interstitial spheres (IS). The band structure spanning the main directions of the base-centered orthorhombic Brillouin zone is shown in Fig. 3 together with site-projected densities of states (PDOS). Along the y axis the energy is with respect to the Fermi level. Within the valence band (VB) below E_F , the relative dispersion of the bands signals the nature of the states involved, thus contrasting lower-energy, largely dispersed *s*, *p*-like bands with highly localized *f* bands around E_F . The intermediate dispersion of the bands at ~ -4 eV corresponds to the *d* states. The conduction band (CB) with empty states also shows dispersion as in the VB. The quantum mixing between the valence states is mainly through the itinerant electrons found in the dispersed bands, *i. e.* in contrast to strongly localized states such as Pd (*4d*) at ~ -4 eV and Ce (*4f*) at E_F . The large intensity of the latter signals a magnetic instability towards spin polarization, *i. e.* a finite magnetization should develop on cerium in SP calculations [31]. This actually occurs when two spin channels (\uparrow and \downarrow) are allowed first in an implicit SP-F configuration, *i. e.* without accounting for two magnetic subcells as shown below. The result of the self-consistent calculations is the actual

onset of a small magnetic moment of $0.37 \mu_B$ (spin-only) concomitant with a trivalent character of cerium. The small magnetic exchange leading to the small moment is illustrated by the site- and spin-projected DOS in Fig. 4 where the energy shift between \uparrow and \downarrow spins is small and is shown mainly for Ce, whereas the two DOS sub-panels nearly mirror each other. The energy stabilization with respect to former NSP calculations is then small: $\Delta E(\text{SP-NSP}) = -0.03$ eV per cell. Considering two magnetic subcells by splitting the Ce, Pd, Ga1, and Ga2 sites into SPIN UP and SPIN DOWN subcells where UP and DOWN spin populations are imposed, leading to AF ordering between the planes, a further energy stabilization occurs with $\Delta E(\text{SP-AF-SP-F}) = -0.01$ eV per cell.

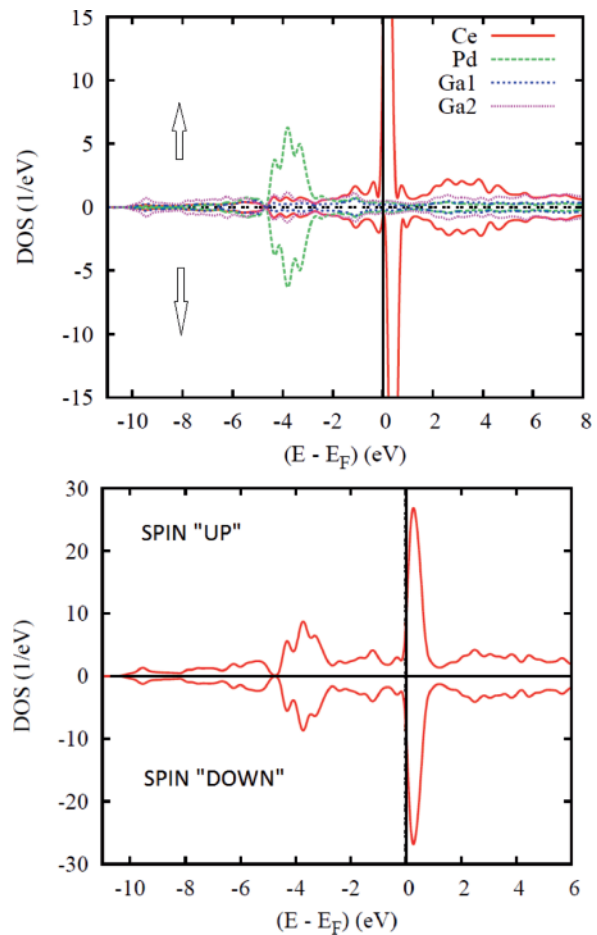


Fig. 4 (color online). DOS of spin-polarized (SP) calculations of $CePdGa_3$: (top) ferromagnetic (SP-F) configuration; (bottom) antiferromagnetic (SP-AF) ground state.

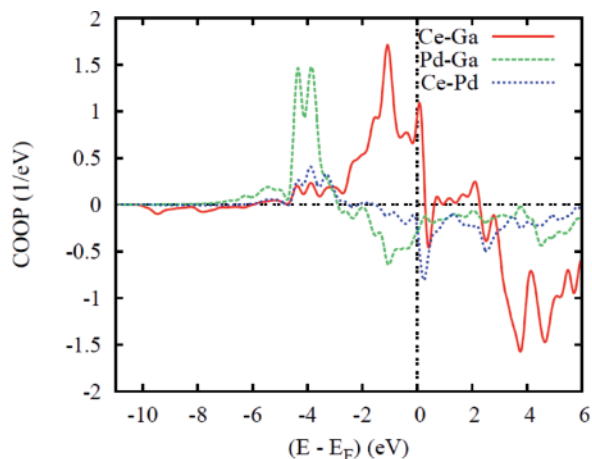


Fig. 5 (color online). Chemical bonding for pair interactions in NSP-CePdGa₃ within the COOP criterion.

The moment on Ce changes little with $\pm 0.36 \mu_B$ and null total magnetization with perfectly mirroring the SPIN UP and SPIN DOWN panels in the lower part of Fig. 4.

Finally we analyzed the chemical bonding with the COOP criterion for pair interactions based on NSP calculations because to a major extent spin polarization results in an almost rigid band shift of the DOS. The COOPs are shown for Ce–Ga, Pd–Ga and Ce–Pd pair interactions, regrouping both Ga1 and Ga2 sites. The COOP plots shown in Fig. 5 exhibit four characteristic features:

1. The smallest bonding contributions are observed for Ce–Pd; this is not only due to the relatively large Ce–Pd spacing of 364 pm but also to the involvement of the Ce and Pd valence states with those of Ga.
2. The top of the VB is dominated by Ce–Ga interactions which are of bonding nature and of much larger magnitude and extension than Pd–Ga. The shortest interatomic distance (Table 4) is actually observed for Ce–Ga although there is a large dispersion of distances.
3. The Pd–Ga interactions are of bonding nature around -4 eV with Pd d states but show large anti-bonding COOPs below E_F . This can be explained by the large filling of the Pd d states so that extra electrons from neighboring Ga atoms will go into anti-bonding states. The opposite is observed for Ce whose d and f valence states are only little occupied.

4. The cohesion of CePdGa₃ is mainly due to the Ce–Ga bonding.

Magnetic properties

Magnetic investigations could be performed for all six compounds ($REPdGa_3$, $RE = La-Eu$) and are represented in Figs. 6–12. Table 5 lists the determined properties of all samples with localized moments. Except for LaPdGa₃ and SmPdGa₃ all compounds exhibit Curie-Weiss behavior above certain temperatures. LaPdGa₃ is a Pauli paramagnet, while SmPdGa₃ shows the typical van Vleck paramagnetism. Fitting the reciprocal susceptibility data leads to effective magnetic moments μ_{eff} that fit very well to the theoretical values of the respective free RE^{3+} ions. Only the value of EuPdGa₃ is slightly reduced which is most likely due to a minor impurity phase. The small effective magnetic moment of SmPdGa₃ can be explained by the van Vleck paramagnetism and will be discussed below in detail. The obtained Weiss constants exhibit negative values except for PrPdGa₃ indicating dominant antiferromagnetic interactions in the paramagnetic range. This is in accordance with the observed antiferromagnetic transitions for all compounds. No magnetic frustration is expected, though the values of the Weiss constants of PrPdGa₃ and NdPdGa₃ are smaller than the obtained ordering temperatures.

The magnetic susceptibility of LaPdGa₃ is nearly temperature-independent above 150 K (see Fig. 6). The absolute value in this range is $0.7(1) \times 10^{-4}$ emu

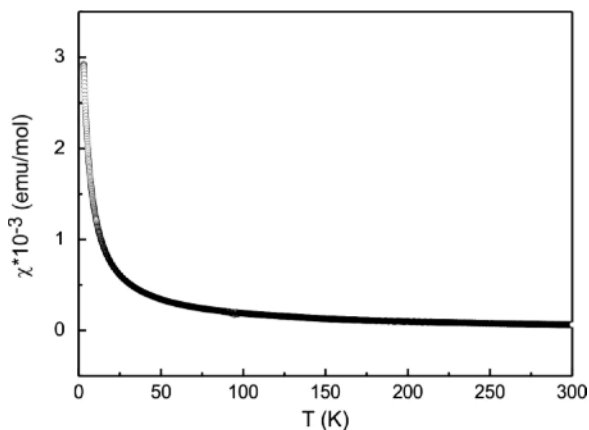


Fig. 6. Temperature dependence of the magnetic susceptibility (χ data) of LaPdGa₃ measured at 10 kOe.

mol^{-1} . Especially below 50 K an upturn of the magnetic susceptibility (Curie tail) can be observed which can be attributed to minor paramagnetic impurities.

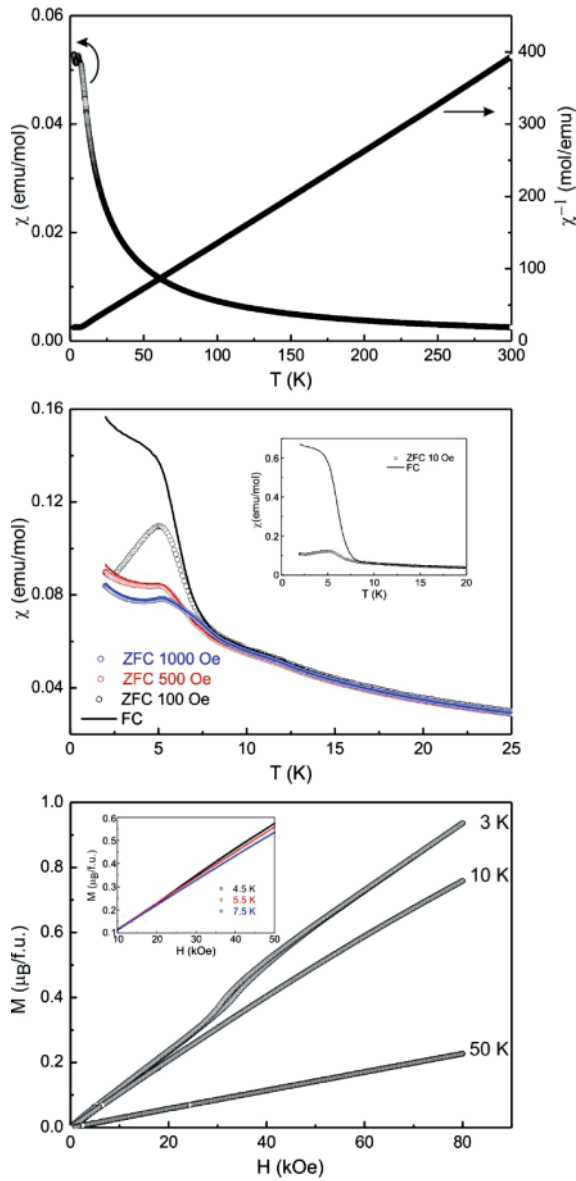


Fig. 7 (color online). Magnetic properties of CePdGa_3 : (top) temperature dependence of the magnetic susceptibility (χ and χ^{-1} data) measured at 10 kOe; (middle) magnetic susceptibility in zero-field-cooled/field-cooled (ZFC/FC) mode at 100, 500 and 1000 Oe in the low-temperature range. The inset presents the ZFC/FC measurement at 10 Oe; (bottom) magnetization isotherms at 3, 10 and 50 K. The inset displays magnetization isotherms at 4.5, 5.5 and 7.5 K.

Consequently, LaPdGa_3 can be described as a Pauli paramagnet. We observed no transition to a superconducting state for this centrosymmetric compound. This is in contrast to several non-centrosymmetric BaNiSn_3 -type superconductors, *e.g.* CeRhSi_3 [32], BaPtSi_3 [33] or SrAuSi_3 [34].

The top panel of Fig. 7 displays the temperature dependence of the magnetic and inverse magnetic susceptibility (χ and χ^{-1} data) of CePdGa_3 measured at 10 kOe. A fit of the χ^{-1} data above 20 K using the Curie-Weiss law, revealed an effective magnetic moment of $\mu_{\text{eff}} = 2.50(1) \mu_B$ per Ce atom and a Weiss constant of $\theta_p = -6.0(1)$ K. The negative value of the Weiss constant points towards weak antiferromagnetic interactions in the paramagnetic range. The effective magnetic moment fits very well to the theoretical value of $2.54 \mu_B$ for a free Ce^{3+} ion and is significantly higher than the observed moment reported by Kwon [35, 36]. This might be a consequence of impurity phases. Furthermore the susceptibility data exhibit an antiferromagnetic ordering around 5 K and a distinct shoulder above this temperature.

To obtain more precise information about these anomalies, low-field measurements with external field strength of 10, 100, 500, and 1000 Oe were performed in a zero-field- and field-cooled (ZFC/FC) mode, which are shown in the middle of Fig. 7. The inset presents the 10 Oe measurement and shows a huge bifurcation between the ZFC and the FC curves, indicat-

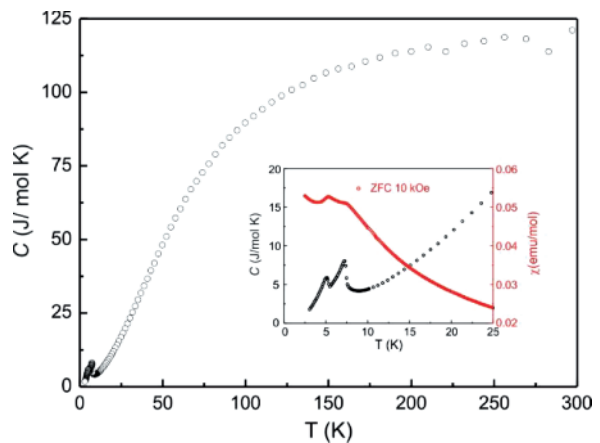


Fig. 8 (color online). Heat capacity of CePdGa_3 measured in the temperature range of 2.0–300 K without an applied field. The inset shows the magnified low-temperature area to highlight two singularities in comparison to the ZFC measurement at 10 kOe.

ing the presence of ferromagnetic interactions. In comparison to the 10 kOe measurement it is conspicuous that only one ordering at 6.0(5) K (determined by the derivative of the FC curve) can be observed which is in between the two anomalies described above. Taken into account the further ZFC/FC curves it is evident that the bifurcation is getting weaker with higher field strength and is not anymore existent at 500 Oe. Additionally, a second anomaly appears, and the kink at around 5 K is getting more pronounced indicating an antiferromagnetic ordering.

The bottom panel in Fig. 7 displays the magnetization isotherms of $CePdGa_3$ measured at 3, 10 and 50 K. The isotherms above the ordering temperature (10 and 50 K) both display a linear field dependency of the magnetization as expected for a paramagnetic material. Only a very weak curvature due to saturation

effects can be observed for the 10 K isotherm. At 3 K the magnetization increases linearly at first, followed by a steep increase at field strength of around 34(3) kOe. This sharp increase can be attributed to a reorientation of the spins, which confirms the antiferromagnetic ground state. A weak hysteresis around this reorientation indicates again the existence of weak ferromagnetic interactions. At higher fields almost no tendency for saturation can be observed, and the magnetic moment at 3 K and 80 kOe ($0.94(5) \mu_B$ per Ce atom) is much lower than the expected saturation magnetization of $2.14 \mu_B$ according to $g_J \times J$. Such reduced magnetization values often occur in cerium compounds and can be attributed to crystal field splitting of the $J = 5/2$ magnetic ground state of Ce^{3+} . Examples are $CeAuGe$ ($1.09 \mu_B$) [37], $CeAgMg$ ($0.66 \mu_B$) [38], or $Ce_3Rh_4Sn_{13}$ ($0.78 \mu_B$) [39].

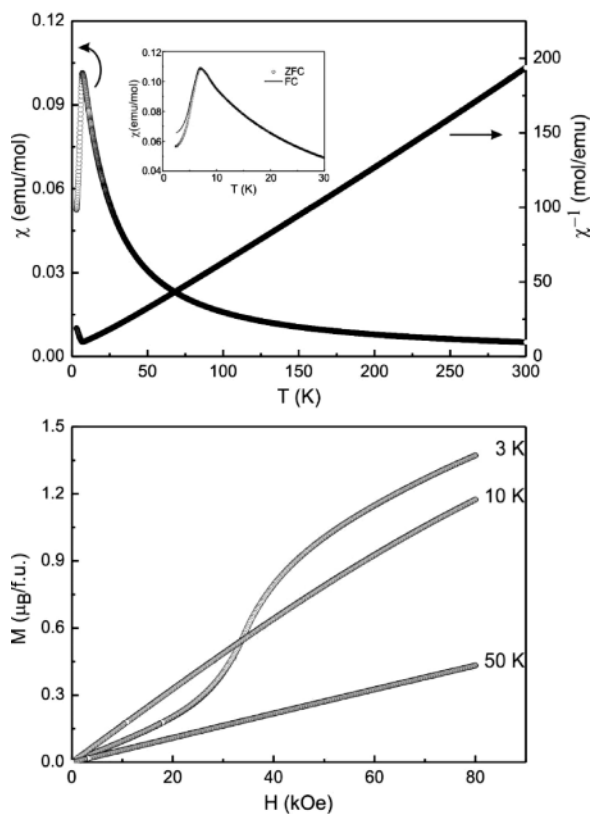


Fig. 9. Magnetic properties of $PrPdGa_3$: (top) temperature dependence of the magnetic susceptibility (χ and χ^{-1} data) measured at 10 kOe. The inset displays the magnetic susceptibility in ZFC/FC mode at 100 Oe; (bottom) magnetization isotherms at 3, 10 and 50 K.

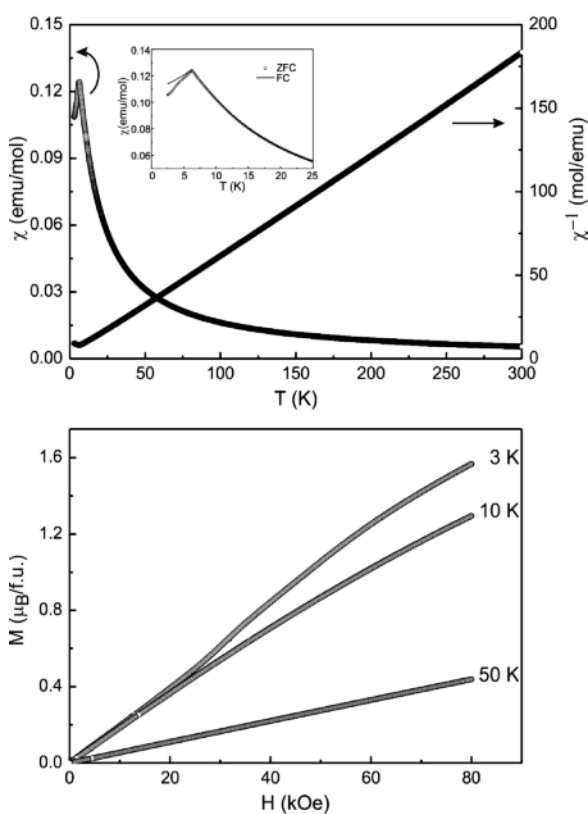


Fig. 10. Magnetic properties of $NdPdGa_3$: (top) temperature dependence of the magnetic susceptibility (χ and χ^{-1} data) measured at 10 kOe. The inset displays the magnetic susceptibility in ZFC/FC mode at 500 Oe; (bottom) magnetization isotherms at 3, 10 and 50 K.

Further isotherms at 4.5, 5.5 and 7 K are shown in the inset. These confirm the antiferromagnetic character of the observed anomaly at 5 K because the reorientation is not anymore existent for the 5.5 K isotherm. In accordance to the theoretical calculations (*vide supra*) the magnetic investigations clearly establish $CePdGa_3$ as antiferromagnet below 5.1(1) K.

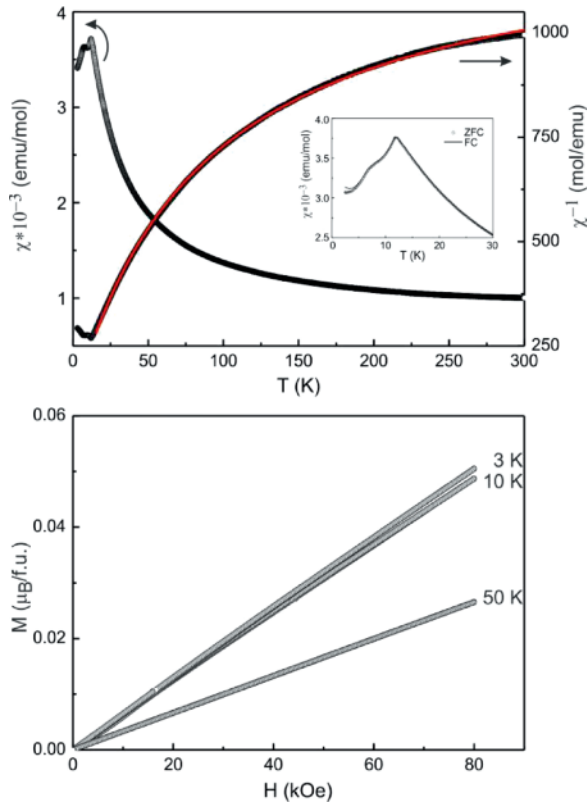


Fig. 11 (color online). Magnetic properties of $SmPdGa_3$: (top) temperature dependence of the magnetic susceptibility (χ and χ^{-1} data) measured at 10 kOe. A fit of the reciprocal susceptibility is presented by the red line (for details see text). The inset displays the magnetic susceptibility in ZFC/FC mode at 100 Oe; (bottom) magnetization isotherms at 3, 10 and 50 K.

A heat capacity measurement of $CePdGa_3$, depicted in Fig. 8, confirms the existence of two anomalies at 5.1(1) and 7.2(1) K. In the inset it is nicely shown that the two anomalies of the 10 kOe ZFC measurement fit very well to the heat capacity data. The second anomaly was also found by Kwon, though their measurement shows a much broader signal [35, 36]. However, we do not believe that the second anomaly is caused by $CePdGa_3$ because all other rare earth com-

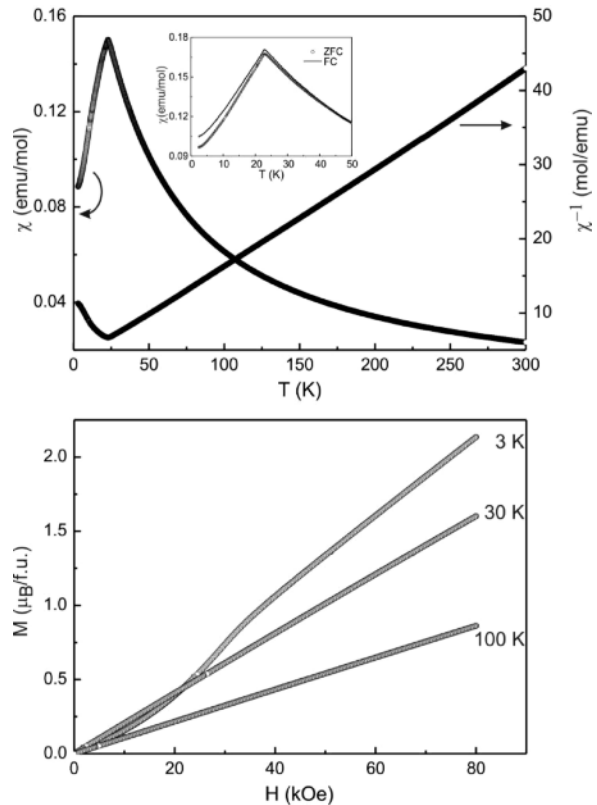


Fig. 12. Magnetic properties of $EuPdGa_3$: (top) temperature dependence of the magnetic susceptibility (χ and χ^{-1} data) measured at 10 kOe. The inset displays the magnetic susceptibility in ZFC/FC mode at 100 Oe; (bottom) magnetization isotherms at 3, 30 and 100 K.

Table 5. Magnetic properties of ternary germanides $REPdGa_3$: μ_{exp} , experimental magnetic moment; μ_{eff} , effective magnetic moment; θ_p , paramagnetic Curie temperature; μ_{sm} , experimental saturation magnetization; $\mu_{sm(calc)}$, calculated saturation magnetization; T_N , Néel temperature.

Compound	μ_{exp} (μ_B / RE)	μ_{eff} (μ_B / RE)	θ_p (K)	μ_{sm} (μ_B / fu)	$\mu_{sm(calc)}$ (μ_B / fu)	T_N (K)
$CePdGa_3$	2.50(1)	2.54	-6.0(1)	0.9(1)	2.14	5.1(5)
$PrPdGa_3$	3.52(1)	3.58	1.5(1)	1.4(1)	3.2	7.0(5)
$NdPdGa_3$	3.63(1)	3.62	-2.3(1)	1.6(1)	3.27	6.3(5)
$SmPdGa_3$	0.70(1)	0.85	-6.4(1)	0.05(1)	0.71	11.9(5)
$EuPdGa_3$	7.77(1)	7.94	-23.1(1)	2.1(1)	7	23.0(5)

pounds exhibits only one antiferromagnetic orientation, and low-field measurements do not show a second singularity. Like described above, the powder pattern of CePdGa_3 exhibits broadened reflections indicating a distribution of domains with compositions $\text{CePd}_{1-x}\text{Ga}_{3+x}$ with a range of small x values. Consequently, we believe that the second anomaly is caused by a slightly different composition.

Like mentioned above further rare earth compounds reveal one antiferromagnetic ordering (Table 5). Except for SmPdGa_3 all samples accomplish a field-induced spin-reorientation at 35(3) (Pr), 34(3) (Nd) and 24(3) (Eu) kOe.

One particularity is the typical van Vleck paramagnetism exposed by SmPdGa_3 due to the proximity of the excited $J = 7/2$ multiplet to the ground $J = 5/2$ multiplet of the Sm^{3+} ions. The energy difference between these states is only about 1550 K, while the other angular momentum levels are correspondingly higher. A very small paramagnetic moment of $0.845 \mu_B$ caused by an antiparallel coupling of the $L = 5$, $S = 5/2$ Russell-Saunders states is observed. Stewart developed a theory for intermetallic samarium compounds which takes account of polarization effects, interionic Heisenberg exchange couplings and the population of the $J = 7/2$ and the $J = 5/2$ ground state. The unexpected simple form $\chi(T) = \chi_0 + D/(T - \theta)$ was found [40]. Hamaker *et al.* proved that $\chi(T)$ for polycrystalline SmRh_4B_4 can be described by the equation

$$\chi_M(T) = \frac{N_A}{k_B} \left[\frac{\mu_{\text{eff}}^2}{3(T - \theta_p)} + \frac{\mu_B^2}{\delta} \right],$$

where μ_{eff} is the effective magnetic moment, θ_p is the Weiss constant, μ_B is the Bohr magneton, N_A is the Avogadro number and k_B is the Boltzmann constant. δ is an energy scale, which is defined as $\delta = 7\Delta E/20$. The first term represents the Curie-Weiss susceptibility of the $J = 5/2$ ground state, while the second part represents the van Vleck susceptibility due to the small energy difference to the $J = 7/2$ multiplet [41]. Using the coefficients for the free ion values mentioned in the literature, this equation can be obtained from a more general one, that was published by Stewart [42, and refs. cited therein]. It should be mentioned that both equations neglect crystal-field splittings of each J level and the mixture of one with another.

By applying the Hamaker equation the data could be described very well with the fit parameters of $\mu_{\text{eff}} = 0.70(1) \mu_B$, $\theta_p = -6.4(5) \text{ K}$ and $\delta = 471(5) \text{ K}$

(see Fig. 11). The effective magnetic moment is less than the $0.845 \mu_B$ of the free ion for the $J = 5/2$ Hund's rule ground state of Sm^{3+} , and $\delta = 471(1) \text{ K}$ corresponds to $\Delta E = 1346 \text{ K}$. This is somewhat lower than the 1550 K predicted by Stewart, but higher than the 1080 K found by Hamaker *et al.* for SmRh_4B_4 [41].

^{151}Eu Mössbauer spectroscopy

The ^{151}Eu Mössbauer spectra of EuPdGa_3 at 78 and 5 K are presented in Fig. 13 together with transmission integral fits. The corresponding fitting parameters are summarized in Table 6. At 78 K, well above the magnetic ordering temperature, the spectrum could be fitted with a single signal at an isomer shift of $-10.24(3) \text{ mm s}^{-1}$, indicative of purely

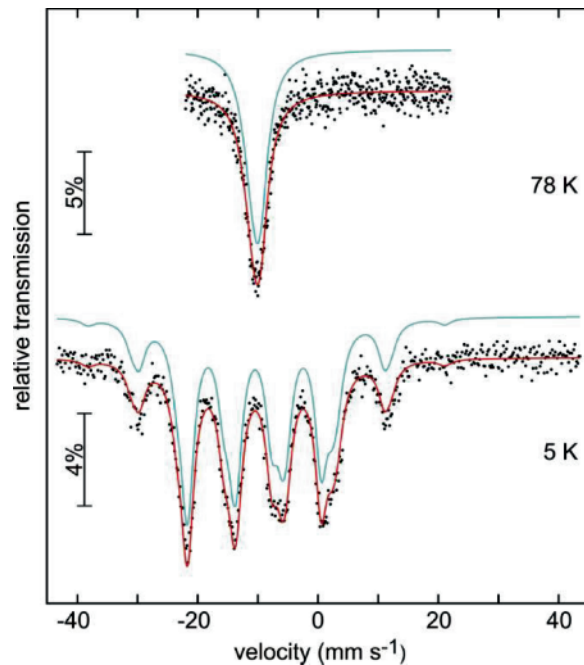


Fig. 13 (color online). Experimental (data points) and simulated (continuous lines) ^{151}Eu Mössbauer spectra of EuPdGa_3 at 78 and 5 K.

Table 6. Fitting parameters of ^{151}Eu Mössbauer spectroscopic measurements of EuPdGa_3 at 78 and 5 K. δ = isomer shift, ΔE_Q = electric quadrupole splitting, Γ = experimental line width, B_{Hf} = magnetic hyperfine field.

T (K)	δ (mm s^{-1})	ΔE_Q (mm s^{-1})	Γ (mm s^{-1})	B_{Hf} (T)
78	$-10.24(3)$	$3.7(3)$	$3.3(2)$	–
5	$-10.19(1)$	$2.05(9)$	$2.48(3)$	$28.7(1)$

divalent europium, in agreement with the susceptibility measurements. A value of $3.7(3) \text{ mm s}^{-1}$ for the electric quadrupole splitting is due to the asymmetric $12 + 5$ coordination of the europium atoms arranged in the cages of the $[\text{GaPd}_3]$ polyanionic network. The experimental line width ($3.3(2) \text{ mm s}^{-1}$) is slightly increased with respect to the typical value of 2.3 mm s^{-1} observed for intermetallic compounds. At 5 K, in the magnetically ordered regime, a magnetic hyperfine field splitting could be observed. The spectrum could be well reproduced by a signal showing

a magnetic hyperfine field of $28.7(1) \text{ T}$, typically observed for europium intermetallics [2, 38, 43].

Acknowledgement

We thank Dipl.-Ing. U. Ch. Rodewald for the intensity data collections. This work was financially supported by the Deutsche Forschungsgemeinschaft through SPP 1458 *Hochtemperatursupraleitung in Eisenpnictiden*. B. G. and O. N. are indebted to the Fonds der Chemischen Industrie and the NRW Forschungsschule *Molecules and Materials – A Common Design Principle* for PhD fellowships.

-
- [1] E. Parthé, L. Gelato, B. Chabot, M. Penzo, K. Cen-zual, R. Gladyshevskii, *TYPIX–Standardized Data and Crystal Chemical Characterization of Inorganic Structure Types*, Gmelin Handbook of Inorganic and Organometallic Chemistry, 8th edition, Springer, Berlin, **1993**.
- [2] D. Kußmann, R. Pöttgen, U. Ch. Rodewald, C. Rosenhahn, B. D. Mosel, G. Kotzyba, B. Künnen, *Z. Naturforsch.* **1999**, 54b, 1155.
- [3] R. Pöttgen, *Z. Anorg. Allg. Chem.* **2014**, 640, 869.
- [4] B. Eisenmann, N. May, W. Müller, H. Schäfer, *Z. Naturforsch.* **1972**, 27b, 1155.
- [5] W. Dörrscheidt, H. Schäfer, *J. Less-Common Met.* **1978**, 58, 209.
- [6] S. Seidel, R.-D. Hoffmann, R. Pöttgen, *Z. Kristallogr.* **2014**, 229, 421.
- [7] Yu. N. Grin, P. Rogl, K. Hiebl, R. Eibler, *J. Less-Common Met.* **1986**, 118, 335.
- [8] P. Hohenberg, W. Kohn, *Phys. Rev.* **1964**, 136, B864.
- [9] W. Kohn, L. J. Sham, *Phys. Rev.* **1965**, 140, A1133.
- [10] R. Pöttgen, T. Gulden, A. Simon, *GIT Labor-Fachzeitschrift* **1999**, 43, 133.
- [11] R. Pöttgen, A. Lang, R.-D. Hoffmann, B. Künnen, G. Kotzyba, R. Müllmann, B. D. Mosel, C. Rosenhahn, *Z. Kristallogr.* **1999**, 214, 143.
- [12] K. Yvon, W. Jeitschko, E. Parthé, *J. Appl. Crystallogr.* **1977**, 10, 73.
- [13] V. Petříček, M. Dušek, L. Palatinus, *Z. Kristallogr.* **2014**, 229, 345.
- [14] R. A. Brand, NORMOS Mössbauer Fitting Program, Universität Duisburg, Duisburg (Germany) **2007**.
- [15] J. P. Perdew, K. Burke, M. Ernzerhof, *Phys. Rev. Lett.* **1996**, 77, 3865.
- [16] A. R. Williams, J. Kübler, C. D. Gelatt, Jr., *Phys. Rev. B* **1979**, 19, 6094.
- [17] V. Eyert, *Int. J. Quant. Chem.* **2000**, 77, 1007.
- [18] V. Eyert, *The Augmented Spherical Wave Method – A Comprehensive Treatment*, Lecture Notes in Physics, Springer, Heidelberg, **2007**.
- [19] P. E. Blöchl, *Phys. Rev. B* **1994**, 50, 17953.
- [20] R. Hoffmann, *Angew. Chem., Int. Ed. Engl.* **1987**, 26, 846.
- [21] J. Emsley, *The Elements*, Oxford University Press, Oxford, **1999**.
- [22] J. Donohue, *The Structures of the Elements*, Wiley, New York **1974**.
- [23] P. Villars, K. Cenzual, *Pearson's Crystal Data: Crystal Structure Database for Inorganic Compounds* (release 2013/14), ASM International®, Materials Park, Ohio (USA) **2013**.
- [24] A. Deschanvres, J. Gallay, J.-M. Hunout, M.-T. Thiault, C. Victor, *C. R. Acad. Sci. C* **1970**, 270, 696.
- [25] G. Giuseppetti, C. Tadini, *Period. Mineral.* **1973**, 42, 335.
- [26] Y. Porter, P. S. Halasyamani, *Z. Naturforsch.* **2002**, 57b, 360.
- [27] I. Oshchapovsky, V. Pavlyuk, G. Dmytriv, A. Griffin, *Acta Crystallogr.* **2012**, C68, i37.
- [28] L. M. Gelato, E. Parthé, *J. Appl. Crystallogr.* **1987**, 20, 139.
- [29] E. Parthé, L. M. Gelato, *Acta Crystallogr.* **1984**, A40, 169.
- [30] Y. Grin, O. M. Sichevich, O. R. Myakush, *Sov. Phys. Crystallogr.* **1991**, 36, 503.
- [31] P. Mohn, *Magnetism in the solid state – An introduction*, Springer Series in Solid-State Sciences, Vol. 134 (Eds.: M. Cardona, P. Fulde, K. von Klitzing, R. Merlin, H.-J. Queisser, H. Störmer), Springer, Heidelberg **2003**.
- [32] N. Kimura, K. Ito, K. Saitoh, Y. Umeda, H. Aoki, T. Terashima, *Phys. Rev. Lett.* **2005**, 95, 247004.
- [33] E. Bauer, R. T. Khan, H. Michor, E. Royanian, A. Grytsiv, N. Melnychenko-Koblyuk, P. Rogl, D. Reith, R. Podloucky, E.-W. Scheidt, W. Wolf, M. Marsman, *Phys. Rev. B* **2009**, 80, 064504.
- [34] M. Isobe, H. Yoshida, K. Kimoto, M. Arai, E. Takayama-Muromachi, *Chem. Mater.* **2014**, 26, 2155.
- [35] J. W. Kim, Y. S. Kwon, *Pysica B* **2006**, 378–380, 833.

- [36] Y. S. Kwon, *Physica B* **2006**, 383, 20.
- [37] R. Pöttgen, H. Borrmann, R. K. Kremer, *J. Magn. Mater.* **1996**, 152, 196.
- [38] D. Johrendt, G. Kotzyba, H. Trill, B. D. Mosel, H. Eckert, Th. Fickenscher, R. Pöttgen, *J. Solid State Chem.* **2002**, 164, 201.
- [39] D. Niepmann, R. Pöttgen, K. M. Poduska, F. J. DiSalvo, H. Trill, B. D. Mosel, *Z. Naturforsch.* **2001**, 56b, 1.
- [40] A. M. Stewart, *Phys. Rev. B* **1972**, 6, 1985.
- [41] H. C. Hamaker, L. D. Woolf, H. P. MacKay, Z. Fisk, M. B. Maple, *Solid State Commun.* **1979**, 32, 289.
- [42] A. M. Stewart, *Phys. Rev. B* **1992**, 47, 11242.
- [43] R. Müllmann, B. D. Mosel, H. Eckert, G. Kotzyba, R. Pöttgen, *J. Solid State Chem.* **1998**, 137, 174.